Biosensors and Bioelectronics 194 (2021) 113592

Contents lists available at ScienceDirect

Biosensors and Bioelectronics

journal homepage: www.elsevier.com/locate/bios

# MRI magnetic compatible electrical neural interface: From materials to application

Yuan Zhang [a,b,c,d,e], Song Le [a,b,c,d,e], Hui Li [f], Bowen Ji [g], Ming-Hao Wang [h], Jin Tao [i], Jing-Qiu Liang [i], Xiao-Yong Zhang [j,k], Xiao-Yang Kang [a,b,c,d,e,*]

[a] Laboratory for Neural Interface and Brain Computer Interface, Institute of AI and Robotics, Academy for Engineering and Technology, FUDAN University, 220 Handan Rd., Yangpu District, Shanghai, 200433, China
[b] Ji Hua Laboratory, 28 Island Ring South Rd., Foshan City, 528200, China
[c] Engineering Research Center of AI & Robotics, Ministry of Education, Shanghai Engineering Research Center of AI & Robotics, MOE Frontiers Center for Brain Science, Shanghai 200433, China
[d] Research Center for Intelligent Sensing, Zhejiang Lab, Hangzhou, 311100, China
[e] Yiwu Research Institute of Fudan University, Chengbei Road, Yiwu City, 322000, Zhejiang, China
[f] Shenzhen Institutes of Advanced Technology, Chinese Academy of Sciences, 1068 Xueyuan Avenue, Shenzhen University Town, Shenzhen, 518055, China
[g] Unmanned System Research Institute; Ministry of Education Key Laboratory of Micro/Nano Systems for Aerospace, School of Mechanical Engineering, Northwestern Polytechnical University, Xi'an, 710072, China
[h] The MOE Engineering Research Center of Smart Microsensors and Microsystems, School of Electronics & Information, Hangzhou Dianzi University, Hangzhou, 310018, China
[i] State Key Laboratory of Applied Optics, Changchun Institute of Optics, Fine Mechanics and Physics, Chinese Academy of Sciences, Changchun, Jilin, 130033, China
[j] Institute of Science and Technology for Brain-inspired Intelligence, FUDAN University, Shanghai, 200433, China
[k] Key Laboratory of Computational Neuroscience and Brain-Inspired Intelligence (Fudan University), Ministry of Education, Shanghai 200433, China

ARTICLE INFO

*Keywords:*
Bioelectronics
Susceptibility
Magnetic resonance imaging (MRI) compatible
Neural interface
Microfabrication
Neural electrode

ABSTRACT

Neural electrical interfaces are important tools for local neural stimulation and recording, which potentially have wide application in the diagnosis and treatment of neural diseases, as well as in the transmission of neural activity for brain-computer interface (BCI) systems. At the same time, magnetic resonance imaging (MRI) is one of the effective and non-invasive techniques for recording whole-brain signals, providing details of brain structures and also activation pattern maps. Simultaneous recording of extracellular neural signals and MRI combines two expressions of the same neural activity and is believed to be of great importance for the understanding of brain function. However, this combination makes requests on the magnetic and electronic performance of neural interface devices. MRI-compatibility refers here to a technological approach to simultaneous MRI and electrode recording or stimulation without artifacts in imaging. Trade-offs between materials magnetic susceptibility selection and electrical function should be considered. Herein, prominent trends in selecting materials of suitable magnetic properties are analyzed and material design, function and application of neural interfaces are outlined together with the remaining challenge to fabricate MRI-compatible neural interface.

## 1. Introduction

With current and emerging neural stimulation and recording technology, the diagnosis and intracranial treatment of neural diseases can be available, especially of those causing motor and sensory disabilities such as epilepsy and Parkinson's disease (PD). Besides, neural activity signals can also be applied to various brain-computer interface (BCI) systems to translate inner thoughts into speeches, images or mechanical controlling instructions. There are different methods for stimulating or recording neural signals, and each has its own merits and demerits. Thus, combining two or more methods can display neural activity multimodally and provide more possibilities for reliable interpretation and analysis of brain functions. Here, the potential and problems of the application to stimulate and record brain activity by implantable electrodes together with magnetic resonance imaging (MRI), especially functional MRI (fMRI), is discussed.

* Corresponding author. Laboratory for Neural Interface and Brain Computer Interface, Institute of AI and Robotics, Academy for Engineering and Technology, FUDAN University, 220 Handan Rd., Yangpu District, Shanghai, 200433, China.
*E-mail address:* xiaoyang_kang@fudan.edu.cn (X.-Y. Kang).

https://doi.org/10.1016/j.bios.2021.113592
Received 25 July 2021; Accepted 24 August 2021
Available online 1 September 2021
0956-5663/© 2021 Elsevier B.V. All rights reserved.

The fMRI is one of the effective and widely-used techniques for recording neural activities, partially due to the advantages of non-invasion, high spatial resolution and the capability of simultaneous acquiring whole-brain signals, which are significant and efficient in the diagnosis of neural diseases and the study of brain functional connections. However, the temporal resolution of fMRI is generally on the order of 100 ms or more, limited by the delayed hemodynamic response function (HRF), instead of the physical property of MRI technology (Logothetis, 2008; Posse et al., 2012; Richter et al., 1996; Shen et al., 2008). Moreover, fMRI signal based on blood-oxygen-level-dependent (BOLD) responses can only represent hemodynamic changes, such as blood volume, and the relationship between BOLD response and neural activity is still concerned and unclear (Logothetis and Panzeri, 2015; Logothetis et al., 2001; Ojemann et al., 2013). Although it has been demonstrated that electroencephalogram (EEG) is one of the potential tools to study neurovascular mechanism (Abreu et al., 2018; Murta et al., 2015; Rosenkranz and Lemieux, 2010; Simões et al., 2015), this noninvasive approach can only record the overall reflection of electrophysiological activities of the whole brain on the scalp surface (Abreu et al., 2018; Buzsaki et al., 2012). In contrast, invasive neural microelectrodes are considered the most convincing sensors to translating electrophysiological signals, because activation of brain site is characterized by action potentials, including single-spike response and local field potential (LFP) (Logothetis et al., 2001). Besides, implanted neural electrodes can also provide controllable electrical stimulation to subjects' brains at a precise site with high resolution, which is efficient and necessary in MRI researches of neural circuits.

On the other hand, the recent developments in implantable neural electrodes were focused on designing a soft and reliable electrode array with a high spatial resolution for chronic application (Patil and Thakor, 2016), and it is essential in chronic implantation to identify the condition and location of implanted neural electrodes by a minimally destructive method (Cogan, 2008; Patil and Thakor, 2016). In such cases, MRI, especially high-field MRI is considered as a potential candidate for positioning reference during and after microelectrode implanting surgery (Li et al., 2017; Foltynie et al., 2011; Jakobs et al., 2018; Rooijen et al., 2013; Verhagen et al., 2016; Walter et al., 2014). At the same time, although microelectrode recording methods have been widely used to collect information about how nerve cells to be activated in anesthetized or alert animals, the data obtained from human researches are limited because of implantation surgeries. Therefore, simultaneously recording electrophysiological signals and fMRI seems to be promising, by which neurovascular coupling can be evaluated, and human brain studies based on MRI and animal researches with microelectrodes can be combined (Hermes et al., 2017; Logothetis et al., 2001; Ojemann et al., 2013).

Additionally, increasing patients with severe neurological diseases were treated with deep brain stimulation (DBS) implants, and these patients have high possibilities to receive MRI after implantation surgeries since MRI has become a routine means of medical diagnostic, not only for neural diseases. According to the patient data in the MarketScan database from 2009 to 2012, it is estimated that approximately 66–75% of DBS-implanted patients may have at least one MRI detection within 10 years of implantation (Falowski et al., 2016). The rate should be even higher with the duration of implantation. This demonstrates the requirement of MRI-compatible DBS implants that should be harmless to patients as well as MR images.

It is not difficult to figure out that there is a necessity to ensure implanted electrodes workable in the MRI environment, or harmless at least. However, simultaneous application of MRI and implanted neural electrodes requires additional safety considerations due to potentially hazardous interactions. First of all, unexpected force on ferromagnetic metal structures may directly cause injuries to implanted sites. Besides, it can be estimated that a conductive implant will be exposed to a time-varying radio frequency (RF) field which forms an eddy current during the MRI process, and potentially causes harmful heating to tissues at the implantation site (Erhardt et al., 2019; Nordbeck et al., 2008; Nyenhuis et al., 2005). Also, currents induced by pulsed gradients may lead to unexpected neural stimulation and enormous electromagnetic artifacts in electrophysiological recording (Oeltermann et al., 2007; Pan et al., 2010). In addition, the magnetic field around neural implants may be distorted, thereby causing artifacts in MRI and precluding observation of the stimulated nucleus (Huang et al., 2015; Schenck, 1996). Worse still, the higher field strength is related to a higher risk of deformation and such error cannot be resolved only by algorithm (Poulen et al., 2020). In order to achieve the MRI-compatible and implantable neural interfaces for neural stimulation or recording, significant improvements have been introduced to MRI-compatible implants, including limited application of ferromagnetic material in implanted device to reduce magnetic force, interference compensation circuits for the gradient noise of MRI during electrophysiological recording, limitation of contact sizes and lead structure to reduce the radiofrequency heating and optimization of MRI parameters for artifacts caused by implantation (Erhardt et al., 2019; Huang et al., 2015; Lloyd et al., 2014; Oeltermann et al., 2007). There were also many interesting pieces of research dealing with the problem of MRI artifacts by selecting MRI-compatible materials and designing special structures of neural electrodes.

Here, we would like to have a review on the intracranial microelectrodes that cause neglectable or no artifacts in MRI to guide the MRI-compatible design of neural electrodes for future development. The cause of MRI artifact and the physical properties that decide MRI-compatibility of materials were described in section MRI-compatible Materials, as well as some studies on the preparation of composites from materials with different properties. Section MRI-compatible Neural Electrode reviewed the recent studies on neural electrodes designed for simultaneous application of electrodes and MRI, classified these studies based on the conductive materials, and compared the electrical properties and MRI artifacts of the neural electrodes. The fourth section Application of MRI-compatible Neural Interface discussed the recent application of MRI-compatible neural electrodes including neural modulation and recording to provide a highlight on the achievements and drawbacks of these MRI-compatible devices.

## 2. MRI compatible materials

The formation of MRI artifacts around implants is due to the magnetic field imperfections, which can also be mentioned as susceptibility effects (Huang et al., 2015). To be specific, any material in a magnetic field will be magnetized and magnetic susceptibility describes the capability of a material to develop a magnetic field of its own when placed in an external magnetic field, related to the microscopic structure of its compositions including the atoms, ions, or molecules. Materials can be classified by the magnitude and sign of susceptibility, as well as their behavior with temperature change. In general, ferromagnetic materials respond strongly to a magnetic field, being attracted to magnets, and cannot be applied in MRI environments, while diamagnetic (negatively susceptible) and paramagnetic (positively susceptible) materials undergo weak magnetization that produces a magnetic field opposite to or in the direction of the local one, respectively. The absolute value of the magnetic susceptibility of an object is positively correlated with the distortion to the external magnetic field. Soft tissues, like the brain, are commonly believed to have a close susceptibility to water, which is about -9.05 ppm (Schenck, 1996).

In an MRI system, a gradient field is applied to build up the linear relationship of location and magnetic field strength, encoding by frequency and phase in an imaging plane (Huang et al., 2015). Hence, any neural implants whose magnetic susceptibility is extremely different from that of tissues will cause distortions in mapping and signal loss consequently (Huang et al., 2015; Morelli et al., 2011; Schenck, 1996). In other words, the variation of susceptibility between an implant and surrounding tissues is highly correlated to MRI quality, especially when the implant is located in the imaging region. As a result, the magnetic

susceptibility should be measured or referred to confirm the compatibility of novel implants for the MRI environment theoretically.

### 2.1. Conductive components

Values of susceptibility of selected conductive materials potentially used in neural implants (in this review, magnetic susceptibility is denoted by volume susceptibility for comparison between different substances and water) have been collected and listed in Table 1, as a reference for selecting MRI-compatible materials. Ideally, if its susceptibility is equally to tissues at the implantation site, an implant will not introduce any artifacts to MRI scanning. However, susceptibility differences between most of the materials in Table 1 and tissues are larger than 10 ppm, possibly causing notorious MRI distortions when metals are implanted (Schenck, 1996). Copper is almost the only single metal for potentially MRI-artifact-free materials ($\chi_{Cu} = -9.6 \times 10^{-6}$), but it is poor in bio-compatibility. Otherwise, graphite and nanostructured carbon materials can be MRI-compatible in a specific structure or direction, but most carbon materials are less conductive than metal and are too fragile to be applied in chronic implantation.

It has been demonstrated that a combination of diamagnetic and paramagnetic materials is capable of narrowing the great gap in the magnetic properties of metal implants and human tissue. Bernd Müller-Bierl et al. investigated diamagnetic coatings of a paramagnetic needle by numerical models as well as experiments with a 1.5 T MRI scanner, indicating that 0.4-mm Bi coating was best for 1.0-mm Ti needle to reduce the size of tip artifacts and the dependency on the orientation of B0 (Muller-Bierl et al., 2005). Fig. 1A, the measured field maps of uncoated and Bi-coated Ti cylinders, showed that the field distortion was reduced due to the coating. Gao Y. et al. suggested that diamagnetic material coating is an effective method to reduce the artifact of MRI generated by paramagnetic implants, and vice versa (Gao et al., 2009, 2010). Based on the magnetic field analysis of the finite element method (FEM), the areas with considerable magnetic disturbance around two dual-material structure model were much smaller than those of one-material models under 1.5 T magnetic field, including one combination of Ti and Bi and the other one of Co–Cr–Mo alloy and graphite.

However, the coating cannot completely compensate for the susceptibility artifacts, especially when a higher spatial resolution of fMRI is required. As a solution, composites of two materials with opposite magnetic susceptibility are thought to potentially have the susceptibility close to that of water. E. Uyama et al. suggested Au-xPt-8Nb alloy fabricated by argon-arc-melting method to be a candidate MRI-artifact-free alloy (Uyama et al., 2010). Kim S. et al. prepared Ti–graphite composites exhibiting a relatively low magnetic susceptibility ($\chi_{Ti-C} = 67.6 \times 10^{-6}$) (Kim et al., 2015). Compared to the one of a pure Ti implant, the MRI image of a Ti-graphite implant inserted into the cow tissue demonstrated that the border between tissue and implant was nearly artifact-free under a magnetic field of 4.7 T and the degree of MRI distortion reduced as graphite added, as shown in Fig. 1B. Due to the high compressive strength and high wear resistance, the Ti-graphite composite was recommended for a patellofemoral knee replacement implant rather than a neural probe. Kodama T. et al. created single-phase and homogeneous Au-Pt alloys with the gradually increasing proportion of Pt, and measured volume susceptibility respectively (Kodama et al., 2017). It was demonstrated in Figs. 1C and 2A that Au-35Pt alloy ($\chi_{Au-35Pt} = -8.8 \times 10^{-6}$) caused artifacts of less than two pixels during MRI, equivalent to copper. Shihoko Inui et al.

**Table 1**
Magnetic susceptibility and Young's module of selected materials used as a conductive part in neural implants.

| Material | Structure | Density (g $cm^{-3}$) | Volume susceptibility (ppm) | Young's Module (GPa) | Bio-toxicity | Ref |
|---|---|---|---|---|---|---|
| Water ($H_2O$)/soft human tissue | – | 1.00 | -9.05 | – | – | (Schenck, 1996; Spees et al., 2001) |
| Human tissue | – | 1.00 to 1.05 | -11.0 to -7.0 | 3 to 20 | – | (Kim et al., 2015; Schenck, 1996) |
| Rat cortex | – | – | -9.39 | – | – | Peprah et al. (2014) |
| Aluminum (Al) | – | 2.75 | 20.7 | 57 to 70 | Toxic | (Huang and Spaepen, 2000; Schenck, 1996; Yu et al., 2018) |
| Bismuth (Bi) | – | 9.75 | -164 | 32 | – | (Kim et al., 2015; Muller-Bierl et al., 2005) |
| Copper (Cu) | – | 8.92 | -9.0 to -10.3 | 110 | Toxic | (Guohai et al., 2018; Kim et al., 2015; Kodama et al., 2017; Schenck, 1996; Zhao et al., 2016) |
| Diamond (C) | – | 3.513 | -21.8 | 1050 | Biosafe | Schenck (1996) |
| Gold (Au) | – | 19.32 | -34 | 47 to 80 | Inert | (Baek et al., 2005; Zhao et al., 2016) |
| Iridium (Ir) | – | 22.65 | 37.66 | 527 | Inert | (Hua and Li, 2011; Martinez Santiesteban et al., 2006) |
| Iridium oxide | – | | 146.89 | | | Martinez Santiesteban et al. (2006) |
| Niobium (Nb) | – | 8.60 | 237 | 103 | Biosafe | (Hua and Li, 2011; Schenck, 1996) |
| Platinum (Pt) | – | 21.45 | 279 | 168 | Inert | (Farraro and McLellan, 1977; Zhao et al., 2016) |
| Silver (Ag) | – | 10.5 | -24 | 63 | Inert | (Huang and Spaepen, 2000; Schenck, 1996) |
| Silicon (Si) | – | 2.33 | -4.2 | 79.8 | Inert | (Hopcroft et al., 2010; Schenck, 1996) |
| Tantalum (Ta) | – | 16.65 | 178 | 186 | Inert | (Hua and Li, 2011; Schenck, 1996) |
| Tin (Sn) | – | 7.3 | -23 | 45 | Biosafe | (El-Ashram, 2006; Schenck, 1996) |
| Titanium (Ti) | – | 4.54 | 174 to 182 | 100 | Inert | (Kim et al., 2015; Kodama et al., 2017; Muller-Bierl et al., 2005; Schenck, 1996) |
| Tungsten (W) | – | 19.35 | 77.2 | 410 | Inert | (Hua and Li, 2011; Schenck, 1996) |
| Zirconium (Zr) | – | 6.49 | 109 | 99.28 | Inert | (Hua and Li, 2011; Kim et al., 2015) |
| Graphite | dimensionless | 2.26 | -204 | 10 | Biosafe | Kim et al. (2015) |
| | perpendicular to atomic planes | – | -595 | – | Biosafe | Zhao et al. (2016) |
| | Parallel to atomic planes | – | -8.3 | – | Biosafe | (Schenck, 1996; Zhao et al., 2016) |
| Ti-C | 30% (vol%) graphite | 3.80 | 67.6 | 81.9 | Biosafe | Kim et al. (2015) |
| Au-Pt | 35% (wt%) Pt | – | -8.8 | – | Inert | (Budworth et al., 1997; Kodama et al., 2017) |
| Au-Nb | 6%(wt%) Nb | – | -10.9 | – | Inert | Inui et al. (2017) |
| Pt-W | 8% (wt%) Ti | – | 65 | – | Biosafe | Kodama et al. (2017) |
| Pt-Ir | 10% (wt%) Ir | – | 231 to 258 | – | Inert | (Budworth et al., 1997; Kim et al., 2015) |
| Carbon nanotube (CNT) | CNT array with infiltration | 0.37 to 0.90 | -5.9 to -8.1 | – | Biosafe | Guohai et al. (2018) |
| | Multiwall carbon nanotubes | – | -26 | 500 to 900 | Biosafe | (Demczyk et al., 2002; Likodimos et al., 2003; Viet et al., 2017; Yu et al., 2018) |

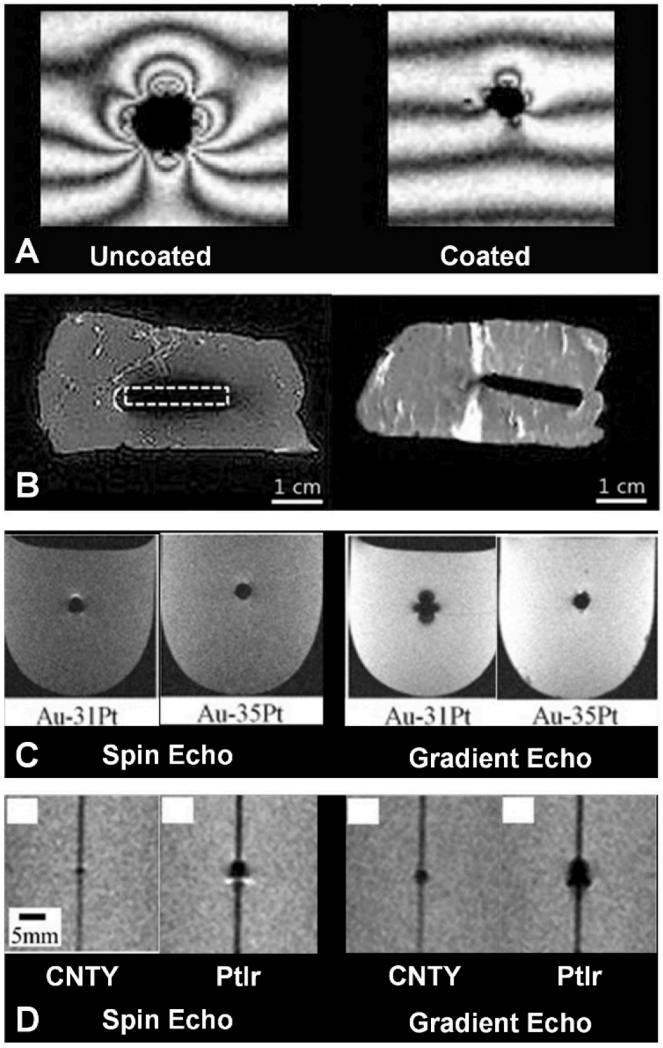


**Fig. 1.** The combination of diamagnetic and paramagnetic materials reduced artifacts in MRI. A) The measured field maps of an uncoated titanium cylinder (left) and a titanium cylinder coated by bismuth (right). The cylinders were 1.0 mm in diameter and the coating layer was 0.4 mm thick. (Reprinted from (Muller-Bierl et al., 2005), Copyright (2004), with permission from WILEY.) B) 4.7 T MR images of cow tissue where the disk of pure Ti (left) and the disk of Ti-30C (vol%) composites (right) were inserted. The disks were 20 mm in diameter and 4 mm in thickness, as shown by dotted lines. (Reprinted from (Kim et al., 2015), Copyright (2015), with permission from Elsevier.) C) MRI images with spin echo and gradient echo sequence of Au-Pt alloy with different components after heat treatment. The sample was 3 mm in diameter and 8 mm in thickness, sunk in agarose gel. (Reprinted from (Kodama et al., 2017), Copyright (2017), with permission from Elsevier.) D) MRI images with spin echo and gradient echo sequence of carbon nanotube yarns and Pt-Ir wires wrapping tightly around polyurethane (PU) tube with a diameter of 1.3 mm at 3.0 T (Jiang et al., 2013). (Copyright © IOP Publishing. Reproduced with permission. All rights reserved.)

investigated the susceptibility of Au-Ta and Au-Nb alloys and alerted that both composition and heat treatment influenced the magnetic property of alloys as long as the Nb contents were larger than 6.8 (Inui et al., 2017). Although they were not eliminated, the artifacts of different alloys with magnetic susceptibility close to tissue were remarkably reduced.

### 2.2. Encapsulating components

However, limited studies have been taken on the application of these MRI-compatible alloys for brain implants. It is probably because components other than contacts and leads will change the magnetic properties of the whole implants, and should also be taken into consideration. For most implantable devices, biocompatibility and chronic stability are determined by the properties of encapsulating or/and substrate materials. Common encapsulating materials include hard ones like ceramic and glass, as well as polymers like polydimethylsiloxane (PDMS, silicone), Parylene and polyimide (PI). However, due to the complicated construction of ceramic and glass structure and the high gas permeability of polymers, encapsulating components usually occupy a certain volume of implants, especially of the thin-film microelectrode array (Scholten and Meng, 2015; Wasikiewicz et al., 2013), and hence, are not negligible when the susceptibility of the whole implants are calculated. Matthias C. Waplera et al. measured the magnetic susceptibility of a large collection of polymers and glasses, providing a useful reference for selecting materials applied in MRI-compatible devices (Wapler et al., 2014). According to the authors, polymethylmethacrylate (PMMA, $\chi_{PMMA} = -7.609 \times 10^{-6} \sim -7.59 \times 10^{-6}$) and PI ($\chi_{PI} = -5.57 \times 10^{-6}$) are recommended as MRI-compatible materials as well as two elastomers which are polyurethane (PU, $\chi_{PU} \approx -8.35 \times 10^{-6}$) and PDMS, whereas some of the materials widely used in neural implants, such as Parylene-C, were not mentioned in the article.

## 3. MRI compatible neural electrode

To improve the MRI-compatibility, some traditional materials and structures have to be modified or even avoided, when neural electrodes are designed, such as Pt-Ir. In most of the related studies, the size and the shape of the electrodes, together with the magnetic susceptibility of the main materials, are considered to have influence on the MRI-compatibility. Here, we summarized the designs of MRI-compatible neural electrodes, and listed their electrical properties and MRI artifacts detected in Table 2.

### 3.1. Size and shape

The size of an object is of importance in determining its MRI-compatibility. In fact, an implant that is much smaller than a voxel in MRI cannot significantly distort the magnetic field for imaging even though it's in the imaging region (Schenck, 1996). Hence, to minimize the artifacts caused by the distortion of the magnetic field in MRI, it is a potential method that the size of implants should be reduced, especially those of great susceptibilities, such as metal leads in neural electrodes. The effect of such reduction is twofold: (a) implants of little size cause less damage to the implantation site during and after surgery, and (b) the smaller neural implants are designed, the less the sum of molecular magnetic moment cause localized distortion. Dongmin Kim et al. developed a 100-nm-thick gold electrode array on a Parylene substrate for rat cortex stimulation to reduce MR signal loss (Kim et al., 2014). Hsin-Yi Lai et al. designed a 50-μm-diameter two-channel tungsten microwire electrode and reported that a T2-weighted structural image demonstrated a reduced artifact with the tungsten electrode, compared with a commercial 75-μm Pt-Ir electrode (PlasticsOne) (Lai et al., 2015). The artifacts around these metal electrodes were reduced but still obvious in echo planar imaging (EPI), which resulted in failures of recording at the implanted sites. However, the size of metal leads in implantable electrodes is also related to the electrical properties, such as conductivity. In other words, minimizing the size of implants might reduce the quality of electric recording signals, which is absolutely undesirable.

At the same time, it should be mentioned that implants with the same susceptibility but different shapes may cause artifacts of different sizes. The bulk magnetic susceptibility (BMS) shift is used to describe the combined influence of susceptibility and shape factor on the observed

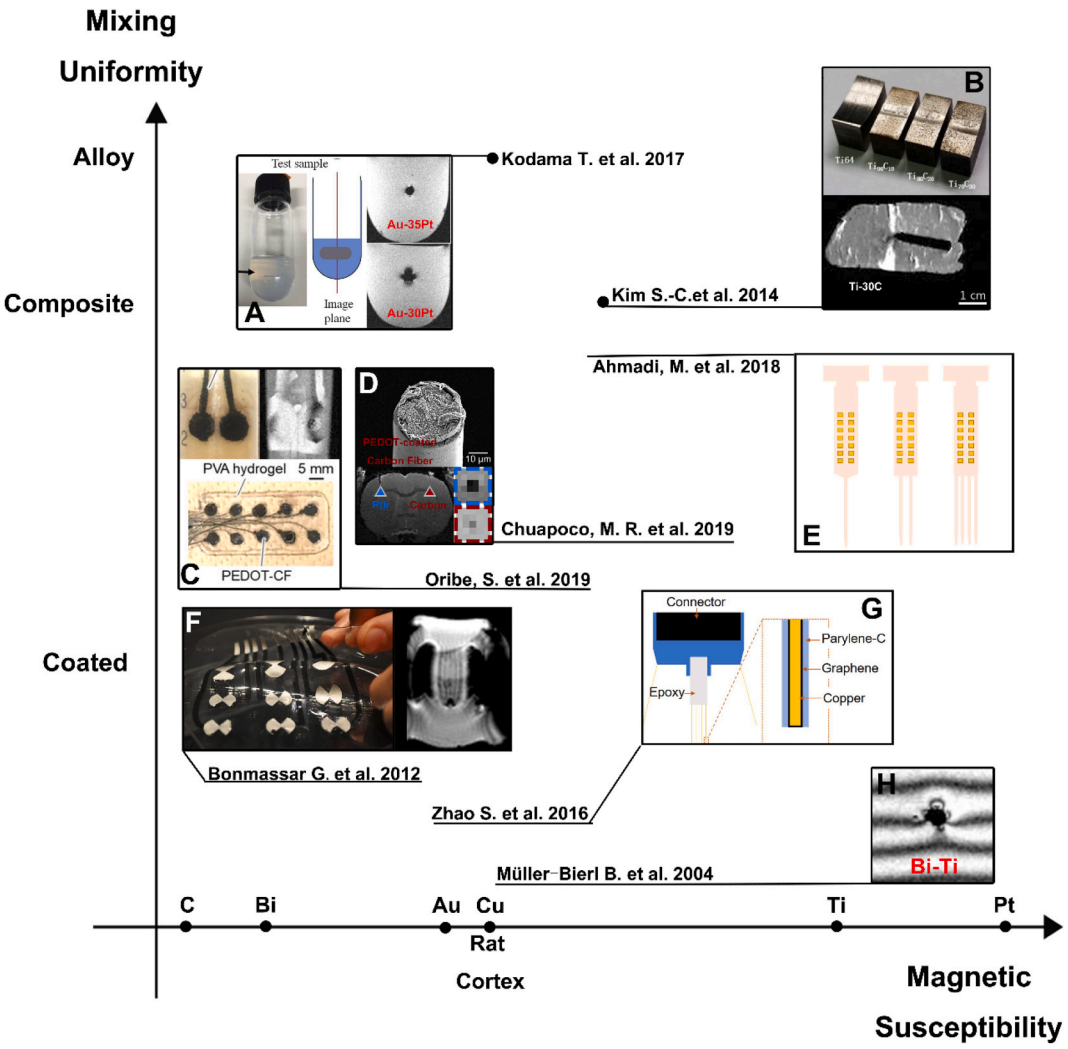


**Fig. 2.** Mixture of two or more materials can be applied to MRI-compatible electrodes to improve the magnetic or electric properties. The "●" marks the material dimension and the susceptibility, followed by the short reference, respectively. A) The alloy samples at varying Au-Pt mixture ratios were fixed in agarose gel within a test tube. 1.5-T MR images of Au-35Pt (- 8.8 ppm) and Au-30Pt were shown and the artifact length around Au-35Pt was minimum. (Reprinted from (Kodama et al., 2017), Copyright (2017), with permission from Elsevier.) B) (Up) The blocks of composite samples with different graphite contents were fabricated for wear tests. (Down) MR images of cow tissue with the $Ti_{70}$-$C_{30}$ composite inserted. (Reprinted from (Kim et al., 2015), Copyright (2015), with permission from Elsevier.) C) Photographs of a hydrogel-based electrode set consisted of pieces of carbon fiber and PEDOT coating, together with its MRI tomographic measurement on an ex vivo rat brain (Reprinted from (Oribe et al., 2019), Copyright (2019), with permission from Springer Nature). D) (Up) SEM images of carbon monofilament electrode tips after coating of PEDOT:pTS. (Down) MR images of Pt-Ir (blue) and carbon monofilament (red) microwire electrodes in a rat brain or an agarose phantom were obtained by fast-spin echo or multi-gradient echo sequence, respectively. (Reprinted from (Chuapoco et al., 2019), Copyright (2019), with permission from Elsevier.) E) A schematic diagram of single-, double- and four-shank Au-coated Cu electrodes fabricated on a polyimide substrate (Ahmadi et al., 2018). F) (Left) The flexible and absorbable electrode set was made from PTFOS substrate, silver ink electrodes and carbon ink leads. BOLD images (right) of a PTFOS electrode set were acquired, as well as T1-and T2-weighted images. (Reprinted from (Bonmassar et al., 2012), Copyright (2012), with permission from Public Library of Science.) G) A schematic diagram of a four-channel array consisted of graphene encapsulated copper (G-Cu) microwires with a diagram of the electrode tip (Zhao et al., 2016). H) MAGSUS field maps of a titanium cylinder with 1.0 mm diameter, coated with 0.4-mm-thick bismuth perpendicular to the exterior field. (Reprinted from (Muller-Bierl et al., 2005), Copyright (2004), with permission from WILEY.).

shift in nuclear magnetic resonance (NMR), which is non-isotropic and hard to cancel. And hence, using samples with regular cross-sections can simplify the preparation and calculation in susceptibility measurements. However, the shape of implantable electrodes is much more complicated than a testing sample, affecting the bulk magnetic susceptibility and finally the MRI artifacts. According to Bernd Müller-Bierl et al., four shapes of microelectrode tips were investigated by numerical models which were a both-side-flat tip, a one-side-flat tip, a centric-conically-shaped tip and a centric-parabolical-shaped tip of cylinders 1.4 mm in diameter (Muller-Bierl et al., 2005). The research indicated that pointed tips were superior to simply cut ends of cylinders, and centric tips were suggested to cause fewer artifacts compared to the flat tips.

### 3.2. Susceptibility

Selecting conductive materials of close magnetic susceptibility to water is another interesting method to reduce artifacts. It is non-ignorable that not only neural electrodes but also connectors and other implanted components should be MRI-compatible to improve image quality (Martinez Santiesteban et al., 2006). As suggested in Table 1., copper is a potential choice for MRI-compatible metal components of neural stimulation or recording systems, due to the promising magnetic property ($\chi_{Cu} = -9.6 \times 10^{-6}$, close to $\chi_{H_2O} = -9.05 \times 10^{-6}$). However, this application in neural electrodes has always been blocked because of the bio-toxicity of copper. Zhao S. et al. developed a

**Table 2**
Representative properties of selected MRI-compatible neural electrodes.

| Electrode | Size | Electrical properties | Artifacts detected | Ref. |
|---|---|---|---|---|
| Polyvinylidene Fluoride (PVDF) coated carbon-fiber-based electrode | 10–20 mm long and 0.2–0.4 mm in diameter | Impedance was 5–20 Ω | ~ 300 μm artifact in a GE FLASH image at 9.4 T (in vivo). | Dunn et al. (2009) |
| Absorbable and stretchable electrode set consisted of polymer thick film organic substrate (PTFOS), electrodes made of silver ink and leads made of carbon ink | 100 mm × 125 mm gelfilm and 265 $mm^2$ electrode area | Resistivity at 126.77 MHz was 2.26 kΩ for the C ink and 0.329 Ω for the Ag ink. | No artifact nor loss of signal was observed in T1 and T2-weighted images (in vitro), as well as in BOLD images (in vivo) | Bonmassar et al. (2012) |
| Carbon nanotube (CNT) yarn electrodes | CNT yarns tightly wrapping around PU tube with a diameter of 1.3 mm (CNTYs were about 50 μm in diameter.) | Impedance was 71 Ω at 1 kHz<br>[a]CSC was 98.6 mC/$cm^2$ | The artifacts reduced 62% and 74% on GE and SE images, compared to the Pt–Ir electrode at 3.0 T (in vitro). | (Guo et al., 2015; Jiang et al. 2011, 2013) |
| Three-channel gold electrode array on a Parylene substrate | 2-μm thick | Not mentioned | Little artifacts or signal loss in T2-weighted MRI (in vivo) at 7.0 T. The MR signal intensity decreased by 4.8% due to gold electrodes. | Kim et al. (2014) |
| Two-channel PI insulated tungsten microwire electrode | 3 cm long, 50 μm in diameter each channel | Impedance was 18 and 22 kΩ at 1 kHz | a greatly reduced artifact in T2-weighted anatomical image at 9.4 T (in vivo) | Lai et al. (2015) |
| Quadri-polar PFA-coated Pt-Ir wires DBS electrode | 140 μm in diameter each electrode | Impedance did not exceed 70 kΩ | Artifacts affected the quality of EPI at 7.0 T around the electrode. | Van Den Berge et al. (2015) |
| Carbon fiber (CF) optrodes (electrode made of 250 or 1000 carbon filaments) | (1K CF) 283 ± 11.6 μm in diameter | (1K CF) Impedance was 28.9 ± 1.6 kΩ | a similar artifact to that of 50-μm-diameter tungsten electrode in structural (FSE) and functional GRE imaging at 7.0 T. | Duffy et al. (2015) |
| Graphene encapsulated copper microwire electrode | 100 μm in diameter | Impedance was ~150 kΩ at 1 kHz | ~150 μm artifacts in diameter in the T2*-weighted image, barely visible in T1- and T2-weighted image at 7.0 T (in vivo) | Zhao et al. (2016) |
| Multiwalled CNT film electrode | (CNT film) 4–8.3 μm thick (CNT electrode) more than 300 μm wide | Not mentioned | Little to no artifact was observed in structural MRI at 9.4 T (in vitro)<br>The apparent width of most of the electrode was approximately 400 μm in GEMS imaging at 9.4 T. (in vivo) | Cruttenden et al. (2017) |
| Infiltrated CNT disk electrodes | 3 mm in diameter | Resistivity was around 1 Ω cm;<br>CSC was between 3.4 and 38.4 mC/cm2; | Susceptibility was −5.9 to −8.1 ppm, measured on PPMS-VSM at 310 K. | Guohai et al. (2018) |
| Single, double or four-shank PI-based Au-coated Cu flexible neural probe | The shank width at the tip is 150 μm, pitch 500 μm | Not mentioned | One-voxel enlargement was observed in high-resolution GEMS imaging at 9.4 T. (in vitro) | Ahmadi et al. (2018) |
| PEDOT coated Carbon monofilament electrodes | The carbon monofilament was 34.5 μm in diameter. | CMEs with no PEDOT:pTS coating had similar impedance to Pt-Ir electrodes. | The average signal intensity of the carbon monofilament microwire never fell below 70% of the undisturbed signal | Chuapoco et al. (2019) |
| Four-channel Parylene-C-insulated carbon nanotube fiber electrode | 10–25 μm in diameter | (20-μm CNT fiber treated with nitric acid)<br>Impedance was 279.96 ± 32.08 kΩ at 1 kHz;<br>CSC was 419.87 ± 73.04 mC/$cm^2$;<br>[b]CIL was 5.04 ± 0.22 mC/$cm^2$. | (20-μm single CNT fiber) artifact size of 268.4 ± 29.9 μm (n = 5) in T2-weighted anatomical images at 7.0 T (in vivo) | Lu et al. (2019) |
| Hydrogel-based PEDOT-modified carbon fabric electrode array | 3-mm-in-diameter each electrode, ~1.4 mm thick | The impedance of PEDOT-CF was slightly larger than the Pt at >1 kHz;<br>Capacitance was 70 mF/$cm^2$; | Little artifacts at 1 T, compared to a metal electrode (ex vivo rat brain) | Oribe et al. (2019) |
| Glassy carbon (GC) ground microelectrode for ECoG | a rectangular geometry of 2 cm × 1 cm, with 2-μm-thick GC layer | The conductivity of GC was 6803 S/m | The outline was barely visible in both T1- and T2-weighted images at 3 T (in vitro). | Nimbalkar et al. (2019) |
| PEDOT:PSS neural stimulation electrodes based on PI substrate | 5.80-μm-thick structure | The average impedance was 25.37 kΩ | The electrodes were MR transparent at 3 T (in vitro). | Rathi et al. (2019) |
| Graphene fiber (GF) electrodes | ~0.17 mm in diameter | Impedance was 15.1 ± 3.67 kΩ at 1 kHz;<br>CSC was 889.8 ± 158.0 mC $cm^{-2}$;<br>CIL was 10.1 ± 2.25 mC $cm^{-2}$; | ~0.18 ± 0.04 mm artifacts in diameter in T2 anatomical images, ~0.70 ± 0.05 mm in EPI at 9.4 T (in vivo) | Zhao et al. (2020) |
| Gold-aluminum microwire neural electrodes | Two 100-μm-diameter gold wires and two 125-μm-diameter aluminum wires twisted together | Conductance was over 2 $M\Omega^{-1}$ (impedance was less than 0.5 MΩ) for each channel; | Up to 0.85 mm artifacts in GEMS and up to 1.25 mm in GRE-EPI (in vivo) | Cruttenden et al. (2021) |

[a] Charge storage capacity.
[b] Charge injection limit.

graphene encapsulated copper (G-Cu) microelectrode, as shown in Fig. 2G (Zhao et al., 2016). According to the histology studies, the cytotoxicity of copper was remarkably weakened by graphene coating. Besides, the size of artifacts induced by the 100-μm G-Cu electrode implanted into a rat's brain was approximately 150 μm in T2*-weighted MRI under 7.0 T. Ahmadi M. et al. designed single, double or four-shank flexible neural probes made of copper on PI substrate [38]. 20-nm gold was deposited on the top of copper to protect brain tissue, and artifacts of the probes were within one voxel in high-resolution gradient echo multiple slice (GEMS) MRI at 9.4 T in agar phantom (Ahmadi et al., 2018). Coating was an effective method to reduce the bio-toxicity of copper, but it will also alter both the electrical and magnetic properties of the neural interface.

Carbon materials have been applied to developing the contacts of neural microelectrodes, including graphite, graphene, carbon nanotube, and so on. It is because the large surface area of porous structure makes the implanted neural interface have a high charge-storage-capacity and also a high charge-injection-limit. At the same time, carbon materials of one- or two-dimension, like carbon nanotube (CNT) and graphene show the potential of MRI-compatibility. A twisting and shrinking method and 65% $HNO_3$ treatment were suggested to convert CNT arrays into yarns and improve the electrochemical properties by different research (Guo et al., 2015; Jiang et al. 2011, 2013; Lu et al., 2019). C. Jiang et al. wrapped CNT yarns around a PU tube with a diameter of 1.3 mm as a DBS electrode which had an impedance of 71 Ω and charge storage capacity (CSC) of 98.6 mC/cm$^2$, better than one without acid treatment and Pt-Ir electrode (Jiang et al., 2011). The MRI artifacts of CNT yarn electrode in vitro were 2.9 mm and 1.8 mm under GE and SE sequence, respectively, when electrodes were parallel to B0 field, as shown in Fig. 3H (Jiang et al., 2013). Linlin Lu et al. designed a multi-channel soft

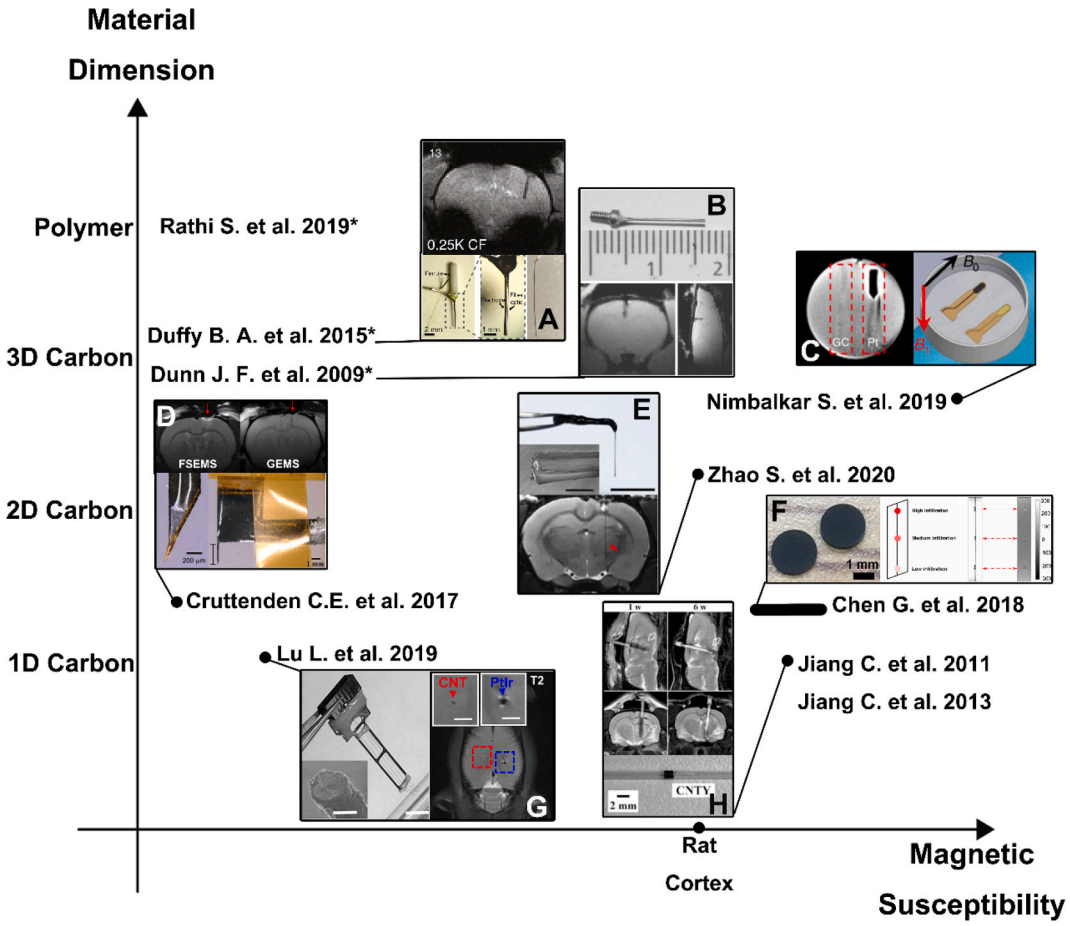


**Fig. 3.** Carbon-based materials are widely applied to MRI-compatible electrodes. The "●" marks the material dimension and the susceptibility, followed by the short reference, respectively. A) (Up) MR image of 0.25K carbon fiber electrode implanted in a rat brain was obtained by spoiled gradient echo sequence. (Down) A carbon fiber electrode and optical fiber were combined using epoxy adhesive. The electrode was made from a 0.25K carbon fiber bundle and coated with PVDF. (Reprinted from (Duffy et al., 2015), Copyright (2015), with permission from Elsevier.) B) (Up) Photograph of a carbon fiber electrode coated with PVDF. (Down) Coronal and sagittal GE FLASH image of the electrode implanted in a rat brain. (Reprinted from (Dunn et al., 2009), Copyright (2008), with permission from WILEY.) C) 3 T T1 -weighted image (left) and diagram (right) of glassy carbon and Pt ground microelectrodes placed on an MRI phantom (Reprinted from (Nimbalkar et al., 2019), Copyright (2019), with permission from Springer Nature). D) (Up) MR images of a rat implanted the CNT electrode were obtained by FSEMS and GEMS at 9.4 T. (Down) The image of carbon Nano-structured electrode and zoomed-in image of the tip. (Reprinted from (Cruttenden et al., 2017), Copyright (2015), with permission from Institute of Physics. E) (Up) The photography of bipolar microelectrode based on graphene fiber. Inset, the SEM image of the electrode tip. (Down) The T2-weighted images of a rat implanted with the microelectrode. (Reprinted from (Zhao et al., 2020), Copyright (2020), with permission from Springer Nature.) F) (Left) A photograph of the CNT electrodes fabricated by CNT forest growth and carbon infiltration. (Right) Diagrams, gradient echo images and field maps of electrodes with different levels of carbon infiltration. (Reprinted from (Guohai et al., 2018), Copyright (2018), with permission from Elsevier.) G) (Left) The image of a four-channel CNT fiber microelectrode array (scale bar, 5 mm) with an SEM image of the fiber tip (scale bar, 10 μm). (Right) The T2-weighted image of a rat brain implanted with a CNT fiber and a Pt-Ir microwire, together with zoomed-in photographs of the implanted sites. (ADAPTED WITH PERMISSION FROM (Lu et al., 2019). COPYRIGHT (2019) AMERICAN CHEMICAL SOCIETY.) H) (Up) T2-weighted images of the CNTY electrode in the rat brains after one-week and six-week implantation. (Down) The CNT yarns were *wrapped* tightly onto a polyurethane (PU) tube, acting as an electrode (Jiang et al., 2013). (Copyright © IOP Publishing. Reproduced with permission. All rights reserved.)

electrode made of CNT fibers with a diameter of 5–20 μm (Lu et al., 2019). Fig. 3G displayed that the 25-μm electrodes made from 20-μm CNT fibers resulted in an artifact size of 268.4 ± 29.9 μm (mean ± SEM, n = 5) in anatomical images at 7.0 T, greatly reducing susceptibility artifacts compared with Pt-Ir electrodes. Layer-by-layer (LBL) nano-assembly methods have been performed by Corey E. Cruttenden et al. to fabricate CNT films that were cut into the desired geometry as an electrode for rat brain studies (Cruttenden et al., 2017). Fig. 3D was the schematic diagram of the CNT film electrode. According to their in-vitro and in-vivo assessment, little to no obvious image loss around the CNT film electrodes was observed in structural MRI at 9.4 T, and the susceptibility of CNT was estimated to be near -30 ppm by simulation. Guohai Chen et al. fabricated carbon nanotubes forest by carbon nanotube templated microfabrication technique and infiltrated with carbon to develop disk electrodes (Fig. 3F) (Guohai et al., 2018). The CNT electrodes had a magnetic susceptibility of −5.9 to −8.1 ppm, close to tissue, and the MRI image of electrodes in vitro demonstrated little distortion in the magnetic field. Zhao S. et al. fabricated 0.18-mm graphene fiber (GF) electrodes with high electrochemical properties, showing little artifact (approximately 0.7 mm in diameter) in EPI image at 9.4 T (Zhao et al., 2020) (Fig. 3E).

Other studies have indicated that a variety of non-nanostructured carbon materials can also effectively reduce the MRI artifacts induced by implants, compared to metal materials. Jeff F. Dunn et al. selected carbon fibers that showed fewer susceptibility artifacts in 9.4 T MRI and developed carbon fiber electrodes coated by nonconductive polymer polyvinylidene difluoride (PVDF), as shown in Fig. 3B (Dunn et al., 2009). Ben A. Duffy et al. attached a carbon fiber electrode to an optical fiber to record LFP-fMRI concurrently in a rat model under optogenetic stimulation (Duffy et al., 2015). Fig. 3A provided the photographs and the in-vivo MRI image of the optrode. When the bundle of approximately 1000 carbon filaments and a 50-μm tungsten electrode were embedded in an agarose phantom, the size of the artifacts was similar in structural MRI at 7.0 T. Giorgio Bonmassar et al. proposed an absorbable and stretchable electrode set consisted of polymer thick film organic substrate (PTFOS), electrodes made of silver ink and leads made of carbon ink, as shown in Fig. 2F, whose electrical properties was similar to standard stainless steel electrodes (Bonmassar et al., 2012). As their researches indicated, there were few artifacts and less signal loss around the PTFOS set in T1 and T2 weighted images, as well as BOLD images, compared to the Pt grid. Besides, carbon micro-electro-mechanical systems technology was introduced to microfabricate glassy carbon (GC) on flexible polymer substrates as ground microelectrode for ECoG in MRI environment, as Surabhi Nimbalkar et al. described (Nimbalkar et al., 2019). Fig. 3C demonstrated the comparison of the GC ground microelectrode and the Pt one, and the GC electrode caused fewer MRI artifacts.

A variety of carbon-based materials have been applied as the conductive components in MRI-compatible implants, but not all of their susceptibilities are close to that of soft tissues. As suggested in Table 1., the susceptibility of carbon is close to that of water when measured in the direction parallel to atomic planes ($\chi_{C\parallel} = -8.3 \times 10^{-6}$), but it differs from that of water in the direction perpendicular to atomic planes ($\chi_{C\perp} = -595 \times 10^{-6}$). We believed that the magnetic susceptibility of carbon is highly related to the dimension of the materials. One- or two-dimensional carbon, like CNT and graphene, has all the atoms on one plane, and so the susceptibility is close to $\chi_{C\parallel}$. In contrast, multi-layer carbon, like graphite, is more affected by magnetic field components perpendicular to the atomic plane, resulting in the susceptibility closer to $\chi_{C\perp}$ than that of graphene. However, the small size of carbon fibers or monofilaments still resulted in smaller artifacts in MRI, and thus the implants can be MRI-compatible.

Although the exact values of susceptibility haven't been measured, as far as know, conductive polymers are also considered to be a candidate as materials of neural electrodes because of the porous surface and bio-compatibility. Shuntaro Oribe et al. developed a stretchable poly (3,4-ethylene dioxythiophene)-modified carbon fabric (PEDOT-CF) electrode array which was embedding into polyvinyl alcohol (PVA) hydrogel substrate in order to reduce the contact impedance on the living tissues, improving the performance in ECoG-fMRI simultaneous recording (Oribe et al., 2019), as shown in Fig. 2C. Chuapoco, M. R. et al. fabricated a PEDOT-CF electrode based on single carbon monofilaments (shown in Fig. 2D) and indicated that a 35-μm-diameter carbon monofilament met the mechanical and magnetic requirements of MRI-compatible electrodes while PEDOT improved the electrical properties (Chuapoco et al., 2019). Sanchit Rathi et al. selected PEDOT-poly (styrene sulfonate) (PEDOT:PSS) to fabricate transparent and MRI-compatible stimulation electrodes based on PI substrate which exhibited MRI-compatibility at 3 T and X-ray imaging compatibility as well (Rathi et al., 2019).

An Au-Al microwire electrode was newly proposed by Corey E. Cruttenden, based on the thought that the combination of a diamagnetic material and a paramagnetic one could reduce the magnetic susceptibility value to that of brain tissue (Cruttenden et al., 2021). The composite four-channel microwire electrode was fabricated by twisting two 100 μm diameter gold wires and two 125 μm diameter aluminum ones. The artifacts of the composite electrodes in GEMS at 16.7 T were less than 0.85 mm, while the artifacts in GRE-EPI were less than 1.25 mm. Although the combination of Au and Al was not homogeous, the artifacts of the electrode were remarkably reduced, compared to the pure gold electrode.

However, there were still limitations that remained in these recent researches. One obstacle is on the way to the application of non-metal materials as neural electrodes, which is their relatively low electrical conductivity and high electrochemical impedance, resulting in poor performance in neural recording. Besides, in most cases of the MRI-compatible and implantable electrode devices mentioned above, the magnetic effect of packaging materials was ignored, when the main conductive materials were carefully selected due to the low magnetic susceptibility. In fact, the packaging materials account for a literarily larger part in some electrode designs such as flexible neural electrode arrays based on thin-film substrates, which highly change the magnetic susceptibility of the whole implants and finally decide the size of artifacts in MRI. At the same time, the coating materials applied for improving the electrochemical performance may also introduce additional artifacts to the implanted site. As a result, the magnetic properties of the implants instead of those of the conductive materials are better indicators of MRI-compatibility.

## 4. Application of MRI-compatible neural electrode

Electrical neural interfaces can provide bidirectional interaction between neurons and external systems, namely neural stimulation and recording. Both of the two interaction modes have their own application scenarios in the MRI environment. The studies based on the simultaneous application of fMRI and neural electrodes have achieved a greater understanding of brain function and also optimized the treatment for some neural diseases. Besides, neural electrodes can be divided into different types according to the implantation sites, and most of the MRI-compatible neural electrodes were designed for the deep brain or cortex. As a result, we have a brief review on researches on the application of MRI-compatible electrodes according to the purpose and the implantation site in this section, hopefully providing some potential ideas for the development of MRI-compatible electrodes and the simultaneous application. Table 3 provided a brief summary of selected studies on the application of MRI-compatible neural electrodes since 2014.

### 4.1. fMRI with electric stimulation

DBS-fMRI studies are popular as an application of MRI-compatible neural electrodes, exploring whole cerebral changes in response to a

**Table 3**
Representative application of MRI-compatible neural electrodes.

| Electrode | Subject | Experiments | Results | Ref. |
|---|---|---|---|---|
| A pair of fine tip glass electrodes filled with artificial cerebrospinal fluid | Rat | [a]LFP -resting-state [b]fMRI | There was a significant correlation between infra low LFP and spontaneous [c]BOLD at recording sites under isoflurane | (Pan et al., 2013; Thompson et al. 2014a, 2014b) |
| A homemade tungsten bipolar microelectrode | Rat | [d]DBS-fMRI | 0.3-mA, 130-Hz, 0.09-ms STN-DBS induces BOLD responses primarily in ipsilateral cortical regions, centered in the motor cortex, collected by EPI scans with 1 s resolution. | Younce et al. (2014) |
| Two-channel gold electrode array on a parylene substrate | Rat | Cortical stimulation-fMRI | 1.2–1.8 mA direct stimulation of the somatosensory cortex induced a negative BOLD signal around the implants, while stimulation of the motor cortex activated distant brain areas of the insular and the thalamus. | Kim et al. (2014) |
| Two-Channel tungsten microwire electrode | Rodent | DBS-fMRI | During VPM-DBS, a positive signal in the somatosensory cortex was caused by stimulation frequencies of 1–40 Hz. | Lai et al. (2015) |
| Strip or depth electrodes | Human | [e]icEEG-fMRI | Some of the observed mesial temporal interictal epileptiform discharge (IED) had a concordant BOLD response in the ipsilateral regions, less than 1 cm from the most active contact. | Aghakhani et al. (2015) |
| Quadri-polar PFA-coated Pt-Ir wires DBS electrode | Rat | DBS-fMRI | Hippocampal DBS evoked a bilateral BOLD response in hippocampal and the mesolimbic network. | Van Den Berge et al. (2015) |
| Carbon fiber optrodes | Rat | LFP recording-fMRI | By optogenetic stimulation of the hippocampus, seizure-like after discharges can be observed by fMRI and LFP recording simultaneously. | Duffy et al. (2015) |
| Subdural surface strip and grid electrodes and penetrating depth electrodes (Ad-Tech) | Human | Cortical stimulation/DBS-fMRI | Stimulation of amygdala, cingulate, or prefrontal cortex safely and reliably evoked activation in distal structures | Oya et al. (2017) |
| A silicon-based linear microelectrode array with 16 gold contacts (Neuronexus) | Rat | LFP recording-fMRI | Concurrent fMRI and LFP recording demonstrated that VTA AMPA microinjection activated dopaminergic neurons in VTA. | Jaime et al. (2018) |
| Glass-coated Pt-Ir wire electrodes with amplifiers consisted of an analog compensation mechanism | Monkey (*Macaca mulatta*) | Single-electrode recording-fMRI | Local injection of Ach in the primary visual cortex caused an increase in BOLD signal and a decrease in LFP near the injection site. | Zaldivar et al. (2018) |
| Grid, strip and depth electrodes or a combination with between 31 and 91 contacts | Human (seizure) | icEEG-fMRI | Automated interictal epileptiform discharge (IED) classification on icEEG-fMRI is developed, with similar concordance to visual classification. | Sharma et al. (2019) |
| Graphene fiber (GF) electrodes | Rat ([f]PD models) | DBS-fMRI | During STN-DBS, a clear "double peak" feature of the BOLD signal in certain regions possibly indicated the involvement of two different circuitries or a delayed neurotransmission effect. | Zhao et al. (2020) |
| Four-channel DBS electrodes (Model L301C, Pins Medical Co.) | Human (PD patients) | DBS-fMRI | Two circuits responded to STN-DBS. One circuit involving GPi was activated and frequency-dependent, while the other circuit involving M1 showed deactivation which was enhanced over time. | Shen et al. (2020) |
| A 16-electrode (4 rows x 4 columns) polyurethane-coated directional DBS lead | Swine | DBS-fMRI | Directional and orientation-selective stimulation in ventrolateral (VL) thalamus modulated activity patterns in the primary motor and somatosensory cortices. | Slopsema et al. (2021) |

[a] Local field potential.
[b] Functional magnetic resonance imaging.
[c] Blood-oxygen-level-dependent.
[d] Deep brain stimulation.
[e] Intracranial electroencephalogram (EEG).
[f] Parkinson's disease.

controllable neural stimulation. The effect of anesthetics, the maintenance of physiological parameters and the stimulation parameters in rodent models, for example, have been studied to develop procedures for DBS-fMRI (Lai et al., 2015; Younce et al., 2014) (Van Den Berge et al., 2015). Directional and orientation-selective electrical stimulation has been introduced to the ventrolateral (VL) thalamus of a swine, providing a different functional response in cortical regions of some individuals depending on lead position and the direction of the electric field (Slopsema et al., 2021). In addition, DBS-fMRI allows researchers to study the acute effects of DBS statistically and the mechanism of the treatments for PD and essential tremor (ET) (Jech, 2008). In the earlier studies, susceptibility artifacts were the main problems, but excitation and inhibition in remote subcortical and cortical areas induced by DBS were observed in fMRI (Jech et al., 2001; Oya et al., 2017; Phillips et al., 2006; Rezai et al., 1999). Recently, with the aid of MRI-compatible electrodes, more deep regions around the implants can be observed and a full activation pattern map can be collected in DBS-fMRI researches, demonstrating neural circuits that have never been observed. For example, in one subthalamic nucleus (STN) DBS study for PD rat models, time-locked "double peak" BOLD signals appeared in the motor cortex, somatosensory cortex, cingulate cortex, and STN, indicating the involvement of two modulation circuits or a delayed neurotransmission effect (Zhao et al., 2020). Another research in PD patients claimed that two neurocircuits responded to STN-DBS (Shen et al., 2020). One circuit involving the globus pallidus internus (GPi), thalamus, and deep cerebellar nuclei was activated and frequency-dependent during stimulation, while the other circuit involving the primary motor cortex (M1), putamen, and cerebellum showed deactivation which was enhanced over time.

Cortical stimulation is another form of direct electrical stimulation. By simultaneously stimulating rodent motor cortex and acquiring fMRI, it has been observed that neuronal activity could propagate from the stimulated region to distant brain areas including the insular and the thalamus (Kim et al., 2014). Similar results can be observed that the human prefrontal cortex was activated time-locked to electrical stimulation on the amygdala (Oya et al., 2017).

### 4.2. Bimodal neural recording

Consistent electrophysiological recording and fMRI data can be used to improve understanding of the relationship between BOLD and neuronal activity. Although many interesting pieces of research have

been conducted based on comparisons between the two modalities, the technical limitations of MRI-compatible electrophysiological recording system led to conducting fMRI and electrical recording asynchronous, introducing variability to the findings (Conner et al., 2011; Mukamel et al., 2005; Ojemann et al., 2013). For concurrent LFP-fMRI studies, Nikos K. Logothetis et al. developed MRI-compatible recording hardware for monkeys including electrodes made of glass-coated $Pt_{90}Ir_{10}$ wires and signal conditioning and active interference compensation system for the gradient noise from MRI scanner, which has been widely applied to the studies on the neurophysiology of BOLD fMRI signals (Goense and Logothetis, 2008; Logothetis et al., 2001; Magri et al., 2012; Oeltermann et al., 2007; Rauch et al., 2008; Zaldivar et al., 2018). Without active interference compensation, electrophysiological signals can be recorded during the hemodynamic response delay based on a priori knowledge of the timing of neuronal events or during the spin recovery period of MRI (Jaime et al., 2018). Different types of stimulation were applied to animals' or humans' brains for LFP-fMRI recording. For example, seizure-like afterdischarges at the whole-brain level and the subthreshold response were investigated under the optogenetic stimulation of the hippocampus of rats by fMRI and optrodes with electrodes based on carbon fibers (Duffy et al., 2015). Other researches turned to pharmacological manipulation for neural stimulation, such as AMPA (α-amino-3-hydroxy-5-methyl-4-isoxazole propionic acid) and acetylcholine (Ach) (Jaime et al., 2018; Zaldivar et al., 2018). Based on experiments of concurrent LFP recording with glass electrodes and resting-state fMRI under different anesthesia, Garth John Thompson and Wen-Ju Pan et al. demonstrated that the spontaneous BOLD signals at the somatosensory cortex and the caudate putamen (CP) significantly correlated to the infra-slow LFP at a delay similar to the hemodynamic response time and the correlation was timing to fMRI-measured quasi-periodic patterns and probably due to neural suppression under isoflurane (Pan et al. 2010, 2013; Thompson et al. 2014a, 2014b).

ECoG or intracranial EEG (icEEG) is thought to be at larger scales of electrophysiological integration in contrast to LFP and MUA, but more sensitive and of higher spatial resolution for deep structures compared to EEG, which may exhibit neural activity in a closer way to fMRI. At the same time, patients with drug-resistant epilepsy are recommended to undergo icEEG monitor, which provides possibilities to study human neural activities via an invasive approach. For instance, the relationship between hemodynamic changes and interictal epileptiform discharges (IED) has been studied by simultaneous icEEG-fMRI recording (Aghakhani et al., 2015), and IED-related BOLD maps based on an automated spike classification algorithm was produced to biologically interpret the generation of IED (Sharma et al., 2019). T. Murta et al. investigated the single-trial correlations between phase-amplitude coupling (PAC) and the BOLD signal via simultaneous icEEG-fMRI in human finger-tapping tasks, and found that the amplitude of BOLD signals was negatively correlated with the PAC strength and the power of the lower EEG frequencies, suggesting that PAC strength explained the variation of BOLD signals (Murta et al., 2017).

## 5. Discussion

A variety of neural interfaces are promising approaches to neural researches as well as diagnosis and treatment for neurological and psychiatric disorders. Among all kinds of neural interfaces, the implantable electrode is a primitive but important tool for both local neural stimulation and recording. However, with the wide application, the defects of existing neural interfaces were exposed, together with some new requirements. Working in an MRI environment has become the challenge faced by neural electrodes since MRI, especially fMRI, developed as one of the most effective techniques for whole-brain recording, but the strong electromagnetic induction phenomenon limits the simultaneous application. Investigation of the MRI-compatibility is a prevailing topic in developing advanced neural electrodes, which was a collection of studies on a range of possible problems in the application. MRI-compatibility, which refers specifically to the capability of supporting artifact-free MRI in this review, can benefits both neuroscience researches and clinical applications, providing possibilities to gather quantitative knowledge on the physiological basis of fMRI, to verify the location of electrode implantation, to evaluating the efficacy of DBS, to meet the need for MRI diagnosis in patients treated with DBS, and so on. The MRI artifact surrounding implants is a signal loss caused by a distorted magnetic field, and hence, the severity of the artifact is mainly determined by the size and shape of implants, the difference of volume magnetic susceptibility between implants and surrounding tissues, as well as field strength, imaging sequence and resolution of MRI. We reviewed the existing MRI-compatible neural electrodes ranging from material preparation to in-vivo verification and application, as guidance for future device development.

It is convincing that the ideal MRI-compatible neural implants that have a homogeneous magnetic field in MRI scanning should be made from materials with the same susceptibility to brain tissues, but a limited number of conductive materials have a susceptibility adapted to the MRI environment. Combining paramagnetic and diamagnetic materials to prepare MRI-compatible materials is effective and can be classified by the mixing uniformity. The coating is a common technique to improve the properties of neural electrodes including impedance, biocompatibility, and mechanical strength, and also an approach to change the magnetic susceptibility in that the absolute value of susceptibility of water is very small and the magnetizations of paramagnetic and diamagnetic materials can cancel each other to get close to that of water. In comparison, an alloy of paramagnetic and diamagnetic materials has a more uniform susceptibility which will achieve artifact-free imaging at a higher spatial resolution. However, the susceptibility of an alloy is related to a variety of factors in processing and the relationships cannot be expressed quantitatively or generally, so most researches only provided one MRI-compatible composite with the optimized component proportions and improved processing parameter for certain pairs of materials and preparation methods. As for electrode design, the recent studies on MRI-compatible neural electrodes have provided a variety of solutions to reduce the size of MRI artifacts caused by the implants to some extent, compared to commercial ones or Pt-Ir electrodes. A large number of the researches were focused on the emerging carbon-based materials due to the excellent biocompatibility and electrochemical surface area, together with the relatively low magnetic susceptibility. Artifacts can also be effectively reduced by developing a neural electrode smaller than MRI resolution, such as the ultra-thin wire electrodes and the microelectrode arrays based on thin-film substrates fabricated by micro-electromechanical system technology. In addition, MRI-compatibility of other components in neural interfaces should also be concerned; otherwise, large artifacts will be induced and thus affect the brain-wide view of MRI. At the same time, eddy currents and harmful heat still require careful considerations in designing an MRI-compatible neural interface, which was not discussed in this review.

Applications of MRI-compatible neural electrodes including electrical stimulation and recording are beneficial to the studies of brain function and the diagnosis and treatment of neural diseases. First of all, once implanted electrodes are visible in MRI, MR-guided implantation and postoperative diagnosis will benefit patients as well as researchers since MRI is generally a safe and noninvasive imaging technique. Another important application is DBS-fMRI, which is an effective approach to improving understanding of the mechanism of neurological diseases such as PD and developing an optimized treatment for patients. With the aid of MRI-compatible electrodes, detailed structure and neural activities at the implantation sites can be visualized by fMRI, and hence functional mapping is accessible to the whole brain. In existing studies, the DBS target is often a single, disease-specific brain region, but DBS-fMRI techniques can be extended to multi-target or different neural conditions. In addition, simultaneous neural recording by fMRI and electrode can verify the physiological basis of BOLD signal, and also build a bridge between the invasive and the non-invasive neural

interfaces. According to the existing studies, BOLD signals in fMRI represent the activation or inhibition of neural activities to a certain extent, but there is still no exact mathematical expression of this mapping relationship. It is possible because the implantation-induced artifact still affected the quality of the EPI in most cases and the electromagnetic interference has not been completely eliminated, which requires further studies. It is also important that the signal quality of the bimodal acquisition is influenced by not only MRI artifacts induced by implants but also electrical artifacts induced by pulsed magnetic fields. As far as known, the electrical artifact can hardly be avoided when the neural signal is collected, but it was usually removed by a data processing algorithm in existing studies.

## 6. Conclusion and outlook

In conclusion, simultaneous application of neural electrodes and MRI is promising and necessary in neurological medicine and research. This review focused on existing studies on materials and neural electrodes that induce little-to-no artifacts in MRI, together with their applications. Although the current electrode designs have already made significant progress and provided unprecedented information about brain functions and brain circuits, the MRI-compatibility of these designs is still incomplete, related to the imaging sequence and other experiment setups. Besides, other potentially hazardous interference should also be comprehensively evaluated, together with MRI artifacts, to advance the wide application of an MRI-compatible neural electrode.

## CRediT authorship contribution statement

**Yuan Zhang:** Investigation, Writing – original draft, Writing – review & editing. **Song Le:** Writing – review & editing. **Hui Li:** Conceptualization, Supervision. **Bowen Ji:** Conceptualization, Supervision. **Ming-Hao Wang:** Conceptualization, Supervision. **Jin Tao:** Conceptualization, Supervision. **Jing-Qiu Liang:** Conceptualization, Supervision. **Xiao-Yong Zhang:** Conceptualization, Supervision. **Xiao-Yang Kang:** Conceptualization, Writing – review & editing, Supervision, Project administration, Funding acquisition.

## Declaration of competing interest

The authors declare that they have no known competing financial interests or personal relationships that could have appeared to influence the work reported in this paper.

## Acknowledgements

The authors acknowledge financial support by the National Natural Science Foundation of China, grant no. 61904038 and no. U1913216; National Key R&D Program of China, grant no. 2021YFC0122702 and no. 2018YFC1705800; Shanghai Sailing Program, grant no. 19YF1403600; Shanghai Municipal Science and Technology Commission, grant no. 19441907600, no.19441908200, and no. 19511132000; Fudan University-CIOMP Joint Fund, grant no.FC2019-002; Opening Project of Shanghai Robot Industry R&D and Transformation Functional Platform, grant no. KEH2310024; Opening Project of Zhejiang Lab, grant no. 2021MC0AB01; Ji Hua Laboratory, grant no. X190021TB190; Shanghai Municipal Science and Technology Major Project, grant no. 2021SHZDZX0103 and no. 2018SHZDZX01; ZJ Lab, and Shanghai Center for Brain Science and Brain-Inspired Technology.

## References

Abreu, R., Leal, A., Figueiredo, P., 2018. Front. Hum. Neurosci. 12, 29.
Aghakhani, Y., Beers, C.A., Pittman, D.J., Gaxiola-Valdez, I., Goodyear, B.G., Federico, P., 2015. Neuroimage Clin. 7, 755–763.
Ahmadi, M., Cruttenden, C., Zhu, X.H., Chen, W., Rajamani, R., 2018. 2018 40th Annual International Conference of the IEEE Engineering in Medicine and Biology Society. EMBC), pp. 4579–4582.
Baek, C.-W., Kim, Y.-K., Ahn, Y., Kim, Y.-H., 2005. Sensor Actuator Phys. 117 (1), 17–27.
Bonmassar, G., Fujimoto, K., Golby, A.J., 2012. PloS One 7 (9), e41187.
Budworth, D.W., Hoare, F.E., Preston, J., 1997. Proc. Roy. Soc. Lond. Math. Phys. Sci. 257 (1289), 250–262.
Buzsaki, G., Anastassiou, C.A., Koch, C., 2012. Nat. Rev. Neurosci. 13 (6), 407–420.
Chuapoco, M.R., Choy, M., Schmid, F., Duffy, B.A., Lee, H.J., Lee, J.H., 2019. Neuroimage 186, 806–816.
Cogan, S.F., 2008. Annu. Rev. Biomed. Eng. 10 (1), 275–309.
Conner, C.R., Ellmore, T.M., Pieters, T.A., DiSano, M.A., Tandon, N., 2011. J. Neurosci. 31 (36), 12855–12865.
Cruttenden, C.E., Ahmadi, M., Zhang, Y., Zhu, X.H., Chen, W., Rajamani, R., 2021. Ann Biomed Eng, pp. 1–12.
Cruttenden, C.E., Taylor, J.M., Hu, S., Zhang, Y., Zhu, X.H., Chen, W., Rajamani, R., 2017. Biomed. Phys. Eng. Expr. 4 (1).
Demczyk, B.G., Wang, Y.M., Cumings, J., Hetman, M., Han, W., Zettl, A., Ritchie, R.O., 2002. Mater. Sci. Eng., A 334 (1–2), 173–178.
Duffy, B.A., Choy, M., Chuapoco, M.R., Madsen, M., Lee, J.H., 2015. Neuroimage 123, 173–184.
Dunn, J.F., Tuor, U.I., Kmech, J., Young, N.A., Henderson, A.K., Jackson, J.C., Valentine, P.A., Teskey, G.C., 2009. Magn. Reson. Med. 61 (1), 222–228.
El-Ashram, T., 2006. Radiat. Eff. Defect Solid 161 (3), 193–197.
Erhardt, J.B., Lottner, T., Martinez, J., Ozen, A.C., Schuettler, M., Stieglitz, T., Ennis, D. B., Bock, M., 2019. Neuroimage 195, 272–284.
Falowski, S., Safriel, Y., Ryan, M.P., Hargens, L., 2016. Stereotact. Funct. Neurosurg. 94 (3), 147–153.
Farraro, R., McLellan, R.B., 1977. Metall. Trans. A 8 (10), 1563–1565.
Foltynie, T., Zrinzo, L., Martinez-Torres, I., Tripoliti, E., Petersen, E., Holl, E., Aviles-Olmos, I., Jahanshahi, M., Hariz, M., Limousin, P., 2011. J. Neurol. Neurosurg. Psychiatr. 82 (4), 358–363.
Gao, Y., Muramatsu, K., Kushibe, A., Yamazaki, K., Chiba, A., Yamamoto, T., 2009. IEEE Trans. Magn. 45 (10), 4837–4840.
Gao, Y., Muramatsu, K., Kushibe, A., Yamazaki, K., Chiba, A., Yamamoto, T., 2010. J. Appl. Phys. 107 (9), 09B323.
Goense, J.B., Logothetis, N.K., 2008. Curr. Biol. 18 (9), 631–640.
Guo, Y., Duan, W., Ma, C., Jiang, C., Xie, Y., Hao, H., Wang, R., Li, L., 2015. Biomed. Eng. Online 14 (1), 118.
Guohai, C., Berg, D., Francis, J., Ileana, H., Eric, F., Wanming, Z., Craig, G., Christopher, P., Davis, R.C., Jeffrey, A., 2018. J. Magn. Reson., S1090780718302076
Hermes, D., Nguyen, M., Winawer, J., 2017. bioRxiv, 083840.
Hopcroft, M.A., Nix, W.D., Kenny, T.W., 2010. J. Microelectromech. S 19 (2), 229–238.
Hua, G., Li, D., 2011. Appl. Phys. Lett. 99 (4), 041907.
Huang, H., Spaepen, F., 2000. Acta Mater. 48 (12), 3261–3269.
Huang, S.Y., Seethamraju, R.T., Patel, P., Hahn, P.F., Kirsch, J.E., Guimaraes, A.R., 2015. Radiographics 35 (5), 1439–1460.
Inui, S., Uyama, E., Hamada, K., 2017. Biomed. Phys. Eng. Expr. 3 (1), 015025.
Jaime, S., Cavazos, J.E., Yang, Y., Lu, H., 2018. J. Neurosci. Methods 306, 68–76.
Jakobs, M., Krasniqi, E., Kloss, M., Neumann, J.O., Campos, B., Unterberg, A.W., Kiening, K.L., 2018. World Neurosurg. 119, e801–e808.
Jech, R., 2008. In: Tarsy, D., Vitek, J.L., Starr, P.A., Okun, M.S. (Eds.), Deep Brain Stimulation in Neurological and Psychiatric Disorders. Humana Press, Totowa, NJ, pp. 179–201.
Jech, R., Urgosik, D., Tintera, J., Nebuzelsky, A., Krasensky, J., Liscak, R., Roth, J., Ruzicka, E., 2001. Mov. Disord. 16 (6), 1126–1132.
Jiang, C., Li, L., Hao, H., 2011. IEEE Trans. Neural Syst. Rehabil. Eng. 19 (6), 612–616.
Jiang, C.Q., Hao, H.W., Li, L.M., 2013. J. Neural. Eng. 10 (2), 026013.
Kim, D., Chin, Y., Reuveny, A., Sekitani, T., Someya, T., Sekino, M., 2014. 2014 36th Annual International Conference of the IEEE Engineering in Medicine and Biology Society, pp. 6702–6705.
Kim, S.C., Lee, H.J., Son, S.G., Seok, H.K., Lee, K.S., Shin, S.Y., Lee, J.C., 2015. Acta Biomater. 12, 322–331.
Kodama, T., Nakai, R., Goto, K., Shima, K., Iwata, H., 2017. Magn. Reson. Imaging 44, 38–45.
Lai, H.Y., Albaugh, D.L., Kao, Y.C., Younce, J.R., Shih, Y.Y., 2015. Magn. Reson. Med. 73 (3), 1246–1251.
Li, B., Jiang, C.Q., Zhang, F., Li, L.M., Ma, Y., 2017. J. Tsinghua Univ. (Sci. Technol.) 57 (9), 952–957.
Likodimos, V., Glenis, S., Guskos, N., Lin, C.L., 2003. Phys. Rev. B 68 (4), 045417.
Lloyd, T., Wedan, S., Stenzel, G., 2014.
Logothetis, N.K., 2008. Nature 453 (7197), 869–878.
Logothetis, N.K., Panzeri, S., 2015. In: Jaeger, D., Jung, R. (Eds.), Encyclopedia of Computational Neuroscience. Springer New York, New York, NY, pp. 1560–1568.
Logothetis, N.K., Pauls, J., Augath, M., Trinath, T., Oeltermann, A., 2001. Nature 412 (6843), 150–157.
Lu, L., Fu, X., Liew, Y., Zhang, Y., Zhao, S., Xu, Z., Zhao, J., Li, D., Li, Q., Stanley, G.B., Duan, X., 2019. Nano Lett. 19 (3), 1577–1586.
Magri, C., Schridde, U., Murayama, Y., Panzeri, S., Logothetis, N.K., 2012. J. Neurosci. 32 (4), 1395–1407.
Martinez Santiesteban, F.M., Swanson, S.D., Noll, D.C., Anderson, D.J., 2006. IEEE Trans. Biomed. Eng. 53 (3), 547–558.
Morelli, J.N., Runge, V.M., Ai, F., Attenberger, U., Vu, L., Schmeets, S.H., Nitz, W.R., Kirsch, J.E., 2011. Radiographics 31 (3), 849–866.
Mukamel, R., Gelbard, H., Arieli, A., Hasson, U., Fried, I., Malach, R., 2005. Science 309 (5736), 951–954.

Muller-Bierl, B., Graf, H., Steidle, G., Schick, F., 2005. Med. Phys. 32 (1), 76–84.
Murta, T., Chaudhary, U.J., Tierney, T.M., Dias, A., Leite, M., Carmichael, D.W., Figueiredo, P., Lemieux, L., 2017. Neuroimage 146, 438–451.
Murta, T., Leite, M., Carmichael, D.W., Figueiredo, P., Lemieux, L., 2015. Hum. Brain Mapp. 36 (1), 391–414.
Nimbalkar, S., Fuhrer, E., Silva, P., Nguyen, T., Sereno, M., Kassegne, S., Korvink, J., 2019. Microsyst. Nanoeng. 5 (1), 61.
Nordbeck, P., Fidler, F., Weiss, I., Warmuth, M., Friedrich, M.T., Ehses, P., Geistert, W., Ritter, O., Jakob, P.M., Ladd, M.E., Quick, H.H., Bauer, W.R., 2008. Magn. Reson. Med. 60 (2), 312–319.
Nyenhuis, J.A., Sung-Min, P., Kamondetdacha, R., Amjad, A., Shellock, F.G., Rezai, A.R., 2005. IEEE Trans. Device Mater. Reliab. 5 (3), 467–480.
Oeltermann, A., Augath, M.A., Logothetis, N.K., 2007. Magn. Reson. Imaging 25 (6), 760–774.
Ojemann, G.A., Ojemann, J., Ramsey, N.F., 2013. Front. Hum. Neurosci. 7, 34.
Oribe, S., Yoshida, S., Kusama, S., Osawa, S.I., Nakagawa, A., Iwasaki, M., Tominaga, T., Nishizawa, M., 2019. Sci. Rep. 9 (1), 13379.
Oya, H., Howard, M.A., Magnotta, V.A., Kruger, A., Griffiths, T.D., Lemieux, L., Carmichael, D.W., Petkov, C.I., Kawasaki, H., Kovach, C.K., Sutterer, M.J., Adolphs, R., 2017. J. Neurosci. Methods 277, 101–112.
Pan, W.J., Thompson, G., Magnuson, M., Majeed, W., Jaeger, D., Keilholz, S., 2010. JoVE 42, 1901.
Pan, W.J., Thompson, G.J., Magnuson, M.E., Jaeger, D., Keilholz, S., 2013. Neuroimage 74, 288–297.
Patil, A.C., Thakor, N.V., 2016. Med. Biol. Eng. Comput. 54 (1), 23–44.
Peprah, M.K., Astary, G.W., Mareci, T.H., Meisel, M.W., 2014. Magn. Reson. Med. 72 (3), 876–879.
Phillips, M.D., Baker, K.B., Lowe, M.J., Tkach, J.A., Cooper, S.E., Kopell, B.H., Rezai, A. R., 2006. Radiology 239 (1), 209–216.
Posse, S., Ackley, E., Mutihac, R., Rick, J., Shane, M., Murray-Krezan, C., Zaitsev, M., Speck, O., 2012. Neuroimage 61 (1), 115–130.
Poulen, G., Chan Seng, E., Menjot De Champfleur, N., Cif, L., Cyprien, F., Perez, J., Coubes, P., 2020. Stereotact. Funct. Neurosurg. 98 (5), 337–344.
Rathi, S., Deckert, M., Brinkhues, S., Detert, M., Shukla, S.M., Brosch, M., Schmidt, B., 2019. IEEE 16th India Council International Conference (INDICON), pp. 1–4.
Rauch, A., Rainer, G., Augath, M., Oeltermann, A., Logothetis, N.K., 2008. Neuroimage 40 (2), 590–600.
Rezai, A.R., Lozano, A.M., Crawley, A.P., Joy, M.L., Davis, K.D., Kwan, C.L., Dostrovsky, J.O., Tasker, R.R., Mikulis, D.J., 1999. J. Neurosurg. 90 (3), 583–590.
Richter, W., Ugurbil, K., Kim, S.G., 1996. Neuroimage 3 (3), S38.
Rooijen, B.D.V., Backes, W.H., Schijns, O.E.M.G., Colon, A., Hofman, P.A.M.J.N., 2013. 73(3).
Rosenkranz, K., Lemieux, L., 2010. Magma 23 (5–6), 309–316.
Schenck, J.F., 1996. Med. Phys. 23 (6), 815–850.
Scholten, K., Meng, E., 2015. Lab Chip 15 (22), 4256–4272.
Sharma, N.K., Pedreira, C., Chaudhary, U.J., Centeno, M., Carmichael, D.W., Yadee, T., Murta, T., Diehl, B., Lemieux, L., 2019. Neuroimage 184, 981–992.
Shen, L., Jiang, C., Hubbard, C.S., Ren, J., He, C., Wang, D., Dahmani, L., Guo, Y., Liu, Y., Xu, S., Meng, F., Zhang, J., Liu, H., Li, L., 2020. Ann. Neurol. 88 (6), 1178–1193.
Shen, Q., Ren, H., Duong, T.Q., 2008. J. Magn. Reson. Imag. 27 (3), 599–606.
Simões, M., Lima, J., Direito, B., Castelhano, J., Ferreira, C., Carvalho, P., Castelo-Branco, M., 2015. 37th Annual International Conference of the IEEE Engineering in Medicine and Biology Society. EMBC), pp. 4065–4068.
Slopsema, J.P., Canna, A., Uchenik, M., Lehto, L.J., Krieg, J., Wilmerding, L., Koski, D.M., Kobayashi, N., Dao, J., Blumenfeld, M., Filip, P., Min, H.K., Mangia, S., Johnson, M. D., Michaeli, S., 2021. Neuroimage 224, 117357.
Spees, W.M., Yablonskiy, D.A., Oswood, M.C., Ackerman, J.J., 2001. Magn. Reson. Med. 45 (4), 533–542.
Thompson, G.J., Pan, W.J., Billings, J.C., Grooms, J.K., Shakil, S., Jaeger, D., Keilholz, S. D., 2014a. Front. Integr. Neurosci. 8, 41.
Thompson, G.J., Pan, W.J., Magnuson, M.E., Jaeger, D., Keilholz, S.D., 2014b. Neuroimage 84, 1018–1031.
Uyama, E., Hamada, K., Honda, E., Asaoka, K., 2010. Iadr General Session.
Van Den Berge, N., Vanhove, C., Descamps, B., Dauwe, I., van Mierlo, P., Vonck, K., Keereman, V., Raedt, R., Boon, P., Van Holen, R., 2015. PloS One 10 (7), e0133245.
Verhagen, R., Schuurman, P.R., van den Munckhof, P., Contarino, M.F., de Bie, R.M., Bour, L.J., 2016. J. Neural. Eng. 13 (6), 066009.
Viet, L., Luo, N., Umer, S., Pawar, R., Zheng, S., 2017. J. Biotechnol. 5, 147–155.
Walter, U., Wittstock, M., Roesche, J., Mueller, J.U., Wolters, A., 2014. 18th International Congress of Parkinson's Disease and Movement.
Wapler, M.C., Leupold, J., Dragonu, I., von Elverfeld, D., Zaitsev, M., Wallrabe, U., 2014. J. Magn. Reson. 242, 233–242.
Wasikiewicz, J.M., Roohpour, N., Vadgama, P., 2013. In: Jaeger, D., Jung, R. (Eds.), Implantable Sensor Systems for Medical Applications, pp. 68–107.
Younce, J.R., Albaugh, D.L., Shih, Y.Y., 2014. JoVE 84, e51271.
Yu, Z., Tan, Z., Fan, G., Xiong, D.-B., Guo, Q., Lin, R., Hu, L., Li, Z., Zhang, D., 2018. Mater. Char. 137, 84–90.
Zaldivar, D., Rauch, A., Logothetis, N.K., Goense, J., 2018. Proc. Natl. Acad. Sci. U. S. A. 115 (51), E12073–E12082.
Zhao, S., Li, G., Tong, C., Chen, W., Wang, P., Dai, J., Fu, X., Xu, Z., Liu, X., Lu, L., Liang, Z., Duan, X., 2020. Nat. Commun. 11 (1), 1788.
Zhao, S., Liu, X., Xu, Z., Ren, H., Deng, B., Tang, M., Lu, L., Fu, X., Peng, H., Liu, Z., Duan, X., 2016. Nano Lett. 16 (12), 7731–7738.